FULL PAPERS

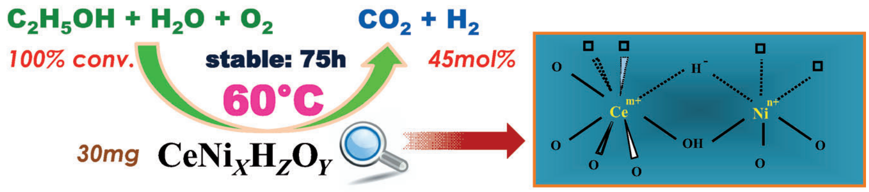

Taking alcohol from the nanobar: $CeNi_XH_ZO_Y$ nano-oxyhydride catalysts enable us to completely convert ethanol at 60 °C and produce hydrogen (45 mol% in the gas phase products) through the oxidative steam reforming reaction. The oxyhydrides are obtained through the in situ activation of $CeNi_XO_Y$ nanocompounds in hydrogen at 250 °C. This technology can save energy by using the strong exothermic chemical reaction between the hydride species in the catalyst and O_2.

*W. Fang, C. Pirez, S. Paul, M. Capron, H. Jobic, F. Dumeignil, L. Jalowiecki-Duhamel**

■■–■■

Room Temperature Hydrogen Production from Ethanol over $CeNi_XH_ZO_Y$ Nano-Oxyhydride Catalysts

DOI: 10.1002/cctc.201300087

Room Temperature Hydrogen Production from Ethanol over $CeNi_XH_ZO_Y$ Nano-Oxyhydride Catalysts

Wenhao Fang,[a] Cyril Pirez,[a] Sébastien Paul,[a, b] Mickaël Capron,[a] Hervé Jobic,[c] Franck Dumeignil,[a, d] and Louise Jalowiecki-Duhamel*[a]

$CeNi_XH_ZO_Y$ nano-oxyhydride catalysts were developed for the highly efficient sustainable hydrogen production from ethanol and water in the oxidative steam reforming reaction. After an in situ treatment in hydrogen in the temperature range of 200–300 °C, the cerium–nickel binary mixed oxides became hydrogen reservoirs, which were called oxyhydrides, in the presence of hydrogen species of the hydride nature in the anionic vacancies of mixed oxides. A novel technology was developed for the room temperature hydrogen production by using the chemical energy released from the reaction between $CeNi_XH_ZO_Y$ nano-oxyhydride catalysts and oxygen, which completely converted ethanol specifically at 60 °C (oven temperature) and simultaneously produced hydrogen, carbon dioxide, and carbon monoxide along with small amounts of methane and ethanal. $CeNi_XH_ZO_Y$ nano-oxyhydride catalysts demonstrated excellent catalytic stability, which was attributed to the graphitic filamentous carbon formed during the reaction. The unique activation phenomenon of the reaction (a huge variation in the temperature between the catalyst bed and the oven) was demonstrated in detail. Finally, the correlations among the catalyst properties, the catalytic performances, and the characterizations were thoroughly discussed.

Introduction

Hydrogen is widely regarded as a promising future energy source to address a series of crisis of the oil shortage, climate change, and environmental pollution, which derives from the exploitation and utilization of fossil fuels.[1–5] Hydrogen energy is critical to any clean energy policy based on its high-energy capacity and environmentally friendliness. Globally, the steam reforming of natural gas, especially methane, is still the most commonly used and the most economically competitive method for H_2 production. To support a clean and sustainable H_2 economy, it is urgently desirable to produce H_2 from renewable energy sources, such as biomass or biomass-derived materials.[6–10] The current mature biomass-fermentation technology makes bioethanol a highly available and low-cost feedstock for H_2 production.[11–13] Of the platform molecules derived from biomass, bioethanol has the advantages of high H_2 content, low toxicity, and ease of delivering. In addition, as bioethanol is a mixture of ethanol and water, it involves water, which is the most renewable, abundant, and cleanest H_2 carrier, in the H_2 generation process, for instance, the steam reforming of ethanol [SRE; Eq. (1)].

$$C_2H_5OH + 3\,H_2O \rightarrow 6\,H_2 + 2\,CO_2 \qquad \Delta H^0{}_{298K} = 174\ \text{kJ mol}^{-1} \tag{1}$$

$$C_2H_5OH + 1.5\,O_2 \rightarrow 3\,H_2 + 2\,CO_2 \qquad \Delta H^0{}_{298K} = -545\ \text{kJ mol}^{-1} \tag{2}$$

In theory, the SRE reaction provides an almost closed carbon recycle because all CO_2 produced during the reforming process can be fed back to biomass through the photosynthesis reaction. In reality, the strongly endothermic SRE reaction is not favorable thermodynamically at low temperatures [Eq. (1)] and essentially requires an extra energy input.[14,15] Such high-temperature operations ($\geq$650 °C) not only consume plenty of energy but also cause inconvenience to the application of H_2 to fuel cells.[16-18] On the contrary, the energy needed can be supplied by adding some O_2 or air to the feed. Thus, the exothermic partial oxidation of ethanol [POE; Eq. (2)] can occur thermodynamically at low temperatures,[11,19,20] during which a portion of ethanol is burned to produce the required energy so as to simultaneously achieve the SRE reaction [Eq. (1)].[1,21-24] In such a context, a technology combining the SRE and POE processes, generally called the oxidative steam reforming of ethanol (OSRE), would be promising for the onboard H_2 production, that is, for the mobile applications that require high H_2 selectivity and rapid response. Moreover, the OSRE reaction could reduce the carbon deposition and thus the addition of

---

[a] W. Fang, Dr. C. Pirez, Prof. Dr. S. Paul, Dr. M. Capron, Prof. Dr. F. Dumeignil, Dr. L. Jalowiecki-Duhamel
Université Lille Nord de France
CNRS UMR8181, Unité de Catalyse et Chimie du Solide
59655 Villeneuve d'Ascq Cedex (France)
E-mail: louise.duhamel@univ-lille1.fr

[b] Prof. Dr. S. Paul
Ecole Centrale de Lille
59655 Villeneuve d'Ascq (France)

[c] Dr. H. Jobic
IRCELyon Institut de Recherches sur la Catalyse et l'Environnement de Lyon
2 Avenue Albert Einstein, 69626 Villeurbanne Cedex (France)

[d] Prof. Dr. F. Dumeignil
Institut Universitaire de France
Maison des Universités
103 Boulevard Saint-Michel, 75005 Paris (France)

O_2 to the feed enables the elimination of carbon on catalyst particles.[25]

The OSRE reaction is generally studied in the catalytic fixed-bed reactors[26–28] or the microchannel membrane reactors.[29–31] The critical factor is the development of highly efficient, stable, and low-cost catalysts, that is, the design of the appropriate active sites that fulfill the above-mentioned features of the OSRE reaction, especially the design of the non-noble metal catalysts.[32–34] Till date, some metal catalytic fixed-bed systems have been reported for the autothermal reforming of ethanol, generally the OSRE reaction, such as the oxide-supported active metal catalysts[11,24,26,27,35] and the Ni-, Co-, and Cu-based mixed oxides.[36,37] There is no doubt that the Ni-based catalyst is the most attractive because of its good activity in the cleavage of the C–C and C–H bonds.[38] However, the drawback of these systems is still reflected in the thermal management. An ideal OSRE process would develop a catalyst working at low temperatures to build long life and safe reformers, which could be used for portable applications.[39,40]

In our previous communication, we reported a novel route for the room temperature H_2 production on the $CeNiH_ZO_Y$ nano-oxyhydride catalyst.[28] This promising technology can save energy by means of a combination of the exothermic reaction between the hydride species stored in the catalyst and O_2 (chemical energy) and the exothermic reaction between ethanol and O_2 (POE reaction). The $CeNiH_ZO_Y$ nano-oxyhydride catalyst can simultaneously activate ethanol, produce H_2 at room temperature, and provide hydride species to sustain the chemical reaction with O_2, which is a remarkable advancement in the field. In our laboratory, $CeNi_XO_Y$ nanocompounds have been studied largely in the SRE reaction because of the strong interactions that exist between the Ni and Ce species in the solid.[15,41–43] As a fluorite-type oxide, CeO_2 has been used in various reactions so as to take advantage of its O_2 storage capacity and/or O_2 diffusion property. The release and uptake of O_2 by CeO_2 enable CeO_2 to participate in the redox reactions, and the increase in the formation of oxygen vacancies attributed to the reduction of Ce cations has been shown to be of importance to catalytic activity.[44,45] A redox process among Ce^{4+}, Ce^{3+}, Ni^0, and Ni^{2+} species has been proposed.[46–49] Thus, the active Ni species in $CeNi_XO_Y$ nanocompounds are characteristically and easily reduced and reoxidized owing to their close interactions with the Ce species.

Not only the $CeNiH_ZO_Y$ (Ni loading 20 wt%) nano-oxyhydride catalyst but also the $CeNi_XH_ZO_Y$ oxyhydride family could demonstrate catalytic activity in the OSRE reaction, which depends on the Ni content. Furthermore, the $CeNi_XH_ZO_Y$ oxyhydrides with various Ni contents have different hydrogen storage capacities in terms of hydride species,[46,47] which are strongly associated with the chemical energy (O_2) consumed to sustain the OSRE reaction at room temperature. For this reason, the effect of the Ni content is likely to bring about interesting catalytic behaviors for the OSRE reaction. Herein, we report the $CeNi_XH_ZO_Y$ oxyhydrides as efficient and stable catalysts for H_2 production from ethanol at room temperature. Complementary to our previous communication, the unique reaction phenomenon (a huge variation in the temperature between the catalytic bed and the oven) is demonstrated in detail in the present study. The correlations among the catalyst properties, the catalytic performances, and the characterizations are discussed to better understand this new technology.

Results and Discussion

Catalytic behavior of the $CeNi_XH_ZO_Y$ nano-oxyhydride catalysts for the OSRE reaction

After an in situ treatment in H_2 at 250 °C, the active $CeNi_XH_ZO_Y$ nano-oxyhydride catalysts obtained are studied for H_2 production from ethanol in the presence of water and O_2. The reactants with a molar composition of $H_2O/EtOH/O_2/N_2 = 3:1:1.6:1.3$ are introduced into the reactor in a specific order (given in the Experimental Section). The reaction can be activated at a certain temperature, from which the temperature of the catalytic bed ($T_{Cat.}$) increases quickly until it can no longer increases within a few minutes. The initial and final temperatures in such an activation phenomenon are recorded as $T_{Ini.}$ and $T_{Fin.}$ At the same moment, the heating supply is lowered to room temperature and the variation in the reaction temperature between the catalytic bed and the oven ($\Delta T_R = T_{Cat.} - T_{Oven}$) is measured precisely when the catalytic system is stable.

The gas phase product distribution in the OSRE reaction on the $CeNi_1H_ZO_Y$ (Ni loading 24 wt%) catalyst are shown in Figure 1 as an example. Complete ethanol conversion is achieved, which is accompanied by the H_2 formation of approximately 45 mol% relative to all the gas phase products (dry basis). The other products analyzed are mainly CO_2 (41 mol%) and CO (12 mol%); small amounts of CH_4 and CH_3CHO are also detected. This is still the best result that has ever been reported for a low-cost catalyst. The reaction temperature ($T_{Cat.}$) is measured at 345 °C, whereas the oven temperature remains at only 60 °C, which is much lower than that required. The energy released from the reaction between the hydride species stored in the oxyhydride catalyst and O_2 (chemical energy) and from the exothermic POE reaction is combined to provide the power necessary to convert ethanol and produce H_2. Thus,

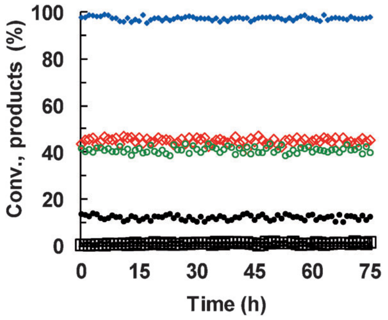

Figure 1. Ethanol conversion and product distribution in the oxidative steam reforming of ethanol reaction on the $CeNi_1H_ZO_Y$ catalyst. Ethanol conversion (◆), H_2 (◇), CO_2 (○), CO (●), CH_4 (▲), and CH_3CHO (□). Reaction conditions: catalyst 30 mg, $H_2O/EtOH/O_2/N_2 = 3:1:1.6:1.3$, $T_{Oven} = 60$ °C, and $T_{Cat.} = 345$ °C.

only a little extra energy is needed to maintain the reaction. The $CeNi_1H_ZO_Y$ catalyst demonstrates excellent catalytic stability after 75 h of the reaction even if a small amount of carbon is formed (with a formation rate of 28 mg h^{-1} $g_{cat}{}^{-1}$) after the reaction. A stable activity in the SRE reaction on such a type of catalyst was attributed to the relatively homogeneous filamentous carbon species formed.[43]

Under the same OSRE conditions, a high and stable conversion of approximately 100 % has already been reported, with the main gas phase products of H_2 (44 mol %), CO_2 (31 mol %), and CO (21 mol %) accompanied by approximately 1 mol % of CH_4 and 3 mol % of CH_3CHO.[28] Herein, the product distribution is improved, which can be probably due to 1) a higher Ni content of 24 wt % and 2) a larger variation in the reaction temperature (ΔT_R). Instead of a $T_{Cat.}$ of 280 °C obtained previously, a higher $T_{Cat.}$ of 345 °C is observed here. The carbon formation rate also decreases compared to the former rate of 63 mg h^{-1} $g_{cat}{}^{-1}$. CO formation rate is also found to decrease, whereas CO_2 formation rate increases.

The ethanol conversion and the gas phase product composition as a function of the Ni content in the OSRE reaction after 20 h are shown in Figure 2. The results obtained in our previous communication are also reported for comparison.[28] Ethanol is completely converted, with an activity constantly higher than 97 % on $CeNi_XH_ZO_Y$ catalysts with various Ni contents. Only small amounts of CH_4 and CH_3CHO are detected in outlet gases. The total molar fraction of these two products decreases slightly with an increase in the Ni content. The other products in the gas phase do not show monotonic change with a change in the Ni content. Approximately 32 % H_2 is formed on the $CeNi_{0.3}H_ZO_Y$ catalyst ($Ni/M_T = 0.23$). Afterward, the H_2 molar fraction increases with the Ni content and reaches an optimum value of approximately 45 % on the $CeNi_1H_ZO_Y$ catalyst. If the Ni/M_T ratio increases to 0.85 ($CeNi_5H_ZO_Y$), H_2 decreases slightly to 40 %. CO formed is approximately 19 % at $Ni/M_T = 0.2$ and reaches the maximum value of 24 % at $Ni/M_T \approx 0.3$, followed by a rapid decrease to approximately 11 % at a higher Ni content. The CO_2 molar fraction presents a minimum at $Ni/M_T \approx 0.4$.

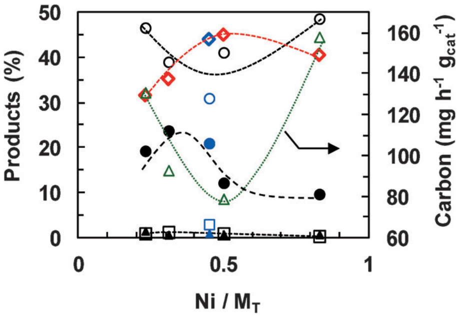

Figure 2. Effect of the Ni content on the oxidative steam reforming of ethanol reaction on $CeNi_XH_ZO_Y$ catalysts. H_2 (◇), CO_2 (○), CO (●), CH_4 (▲), CH_3CHO (□), and carbon formation (△). Reaction conditions: catalyst 30 mg, $H_2O/EtOH/O_2/N_2 = 3{:}1{:}1.6{:}1.3$, $T_{Oven} = 60$ °C, and time 20 h. Ethanol conversion is approximately 100 % independent of the Ni content. For comparison, the result reported in our previous paper is represented by blue symbols.[28]

Complementary to Equations (1) and (2) leading to the formation of H_2 and CO_2, different byproducts can be obtained, owing to the co-occurrence of different reactions that are also involved. For example, ethanol can be decomposed into a mixture of CO, CH_4, and H_2 [Eq. (3)] at a low temperature on the catalysts with a strong capability of the C–C bond rupture, such as the Ni catalyst.[42,43,50] The water-gas shift reaction that is slightly exothermic is favored at low temperature and enables the transformation of CO [Eq. (4)]. The dehydrogenation of ethanol [Eq. (5)] and the decomposition of CH_3CHO [Eq. (6)] can occur at the intermediate temperatures (300–350 °C). Moreover, in the presence of O_2, the partial oxidation of methane [Eq. (7), which is also exothermic] can lead to the formation of H_2 and CO (or CO_2 at a higher O_2 concentration).

$$C_2H_5OH \rightarrow CO + CH_4 + H_2 \tag{3}$$

$$CO + H_2O \rightarrow H_2 + CO_2 \tag{4}$$

$$C_2H_5OH \rightarrow CH_3CHO + H_2 \tag{5}$$

$$CH_3CHO \rightarrow CO + CH_4 \tag{6}$$

$$CH_4 + 0.5\,O_2 \rightarrow CO + 2\,H_2 \tag{7}$$

The amount of carbon formed is measured after the reaction, and it is strongly associated with the Ni content (Figure 2). The $CeNi_1H_ZO_Y$ catalyst forms the smallest amount of carbon with a formation rate of 79 mg h^{-1} $g_{cat}{}^{-1}$ after 20 h of the reaction. With exactly the same catalyst, a much smaller amount of carbon is formed with a formation rate of 28 mg h^{-1} $g_{cat}{}^{-1}$ after 75 h. The result reveals that carbon is not linearly generated with the time on stream; in contrast, the formation rate is relatively in inverse proportion to the reaction time. It indicates that most of the carbon is deposited in the initial stage and may be before introducing O_2. In reality, carbon can be formed through the total decomposition of ethanol. Moreover, solid carbon can also be generated through the disproportionation of CO and/or the decomposition of CH_4.[14,51]

To understand the product distribution, it is necessary to investigate the effect of the Ni content on the activation phenomenon, which plays a dominant role in the OSRE reaction. As shown in Figure 3, when the oven temperature is set at 60 °C, the highest reaction temperature of 345 °C is measured on the $CeNi_1H_ZO_Y$ catalyst whereas the lowest reaction temperature of 301 °C is measured on the $CeNi_{0.3}H_ZO_Y$ catalyst. Notably, no variation in the reaction temperature could be observed under exactly the same reaction conditions without the pretreatment of the catalyst in H_2. Moreover, the total conversion of ethanol is obtained regardless of the Ni content, whereas the variation in the temperature depends on the Ni content. Therefore, the exothermic POE cannot justify the reaction at room temperature. The activation phenomenon is mostly attributed to the exothermic reaction between the hydride species of the solid and O_2. Thus, the variation in the reaction temperature depends on the concentration of the hydrogen

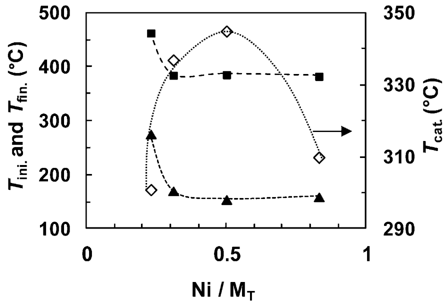

Figure 3. Variation in temperatures versus Ni content in the oxidative steam reforming of ethanol reaction on $CeNi_XH_ZO_Y$ catalysts. $T_{Cat.}$ (◇), $T_{Ini.}$ (▲), and $T_{Fin.}$ (■). Reaction conditions: catalyst 30 mg, $H_2O/EtOH/O_2/N_2=3:1:1.6:1.3$, $T_{Oven}=60\,^{\circ}C$, and time 20 h.

stored in the solid as hydride species. In reality, it has been disclosed by a chemical titration technique that the $CeNi_1O_Y$ nanocompound possesses the highest hydrogen storage capacity among the $CeNi_XO_Y$ series of catalysts.[47,48] The evolution of ΔT_R is found to be quite similar with the curve of H_2 formation versus the Ni content. A part of hydride species are consumed by O_2 to provide enough chemical energy to drive the catalytic reaction at room temperature; meanwhile, the hydride species are generated continuously from ethanol to sustain the reaction.

To explain how the Ni content affects the carbon formation, the initial and final temperatures are investigated during the activation phenomenon (Figure 3). Notably, the reaction can be activated at 155–171 °C on the catalysts with $Ni/M_T \geq 0.5$ after O_2 is added to the feed. In such a case, the final temperatures are recorded entirely at approximately 385 °C. In the case of the lower Ni molar ratio of 0.3, the reaction has to be started at a much higher temperature of 276 °C, although the final temperature is also found to be higher at approximately 463 °C. Of the complete series of catalysts, the $CeNi_1H_ZO_Y$ catalyst still demonstrates the optimum behavior, which gives the largest variation between the initial and final temperatures during the activation phenomenon of the reaction. The variation between the initial and final temperatures is found to obey the similar regulation of ΔT_R. Thus, the $CeNi_1H_ZO_Y$ and $CeNi_{0.5}H_ZO_Y$ catalysts can inhibit the carbon formation, because these catalysts can activate the reaction at lower temperatures (coke formation stage) and drive the reaction at higher temperatures (coke removal and balance stage). On the contrary, the $CeNi_5H_ZO_Y$ and $CeNi_{0.3}H_ZO_Y$ catalysts produce more solid carbon, which can be ascribed to the high Ni content and the much higher initial temperature, respectively. Regardless of the carbon formation rate, the $CeNi_XH_ZO_Y$ series of catalysts all possess excellent catalytic stability.

Characterizations of $CeNi_XO_Y$ catalysts

Analysis by using the Brauner-Emmett-Teller method and inductively coupled plasma-mass spectrometry

The precise Ni loadings and the surface areas of the $CeNi_XO_Y$ nanocompounds were measured and are listed in Table 1. All the mixed oxides have a relatively large surface area, which is no less than 75 m^2g^{-1}; $CeNi_{0.5}O_Y$ and $CeNi_1O_Y$ particularly present the highest specific areas in the range of approximately 110–120 m^2g^{-1}.

Table 1. Ni loading, specific surface area, and crystallite size of $CeNi_XO_Y$ nanocompounds.

Sample	Ni loading [wt %]	Ni/M$_T$	S_{BET} [m^2g^{-1}]	d_{NiO} [nm]	d_{CeO_2} [nm]
$CeNi_{0.02}O_Y$	0.3	0.02	76	–	6
$CeNi_{0.3}O_Y$	7.9	0.23	79	–	5
$CeNi_{0.5}O_Y$	12.2	0.31	109	8	5
$CeNi_1O_Y$	24.0	0.50	119	11	4
$CeNi_5O_Y$	52.8	0.85	84	10	4

Analysis by using XRD

The XRD patterns of the $CeNi_XO_Y$ nanocompounds with various Ni contents are shown in Figure 4. A CeO_2-like phase (JCPDS file 34-0394) with similar intensity is clearly detected in each sample, whereas the NiO phase (JCPDS file 4-0835) starts to emerge at $X \geq 0.5$. Furthermore, the diffraction peaks of crystallized NiO become more intense for the samples with higher Ni content. As already reported, the addition of Ni has an effect not only on the broadness of CeO_2 peaks but also on their positions, which was attributed to the substitution of Ce^{4+} cations with Ni^{2+} cations inside the CeO_2 lattice and was interpreted through the formation of the Ce–Ni solid solution.[46] The ionic radius of the Ni cation (0.07 nm) is smaller than that of the Ce cation (0.09 nm). The $CeNi_XO_Y$ compounds can be ascribed to a mixture of nanoparticles consisting of CeO_2 and NiO and to a solid solution consisting of both Ce and Ni species when $X<1$.[41,42,46] The highest proportion of the solid solution has been found for the $CeNi_{0.5}O_Y$ compound in this series of catalysts.[46] Thus, our current results are in agreement with the literature.

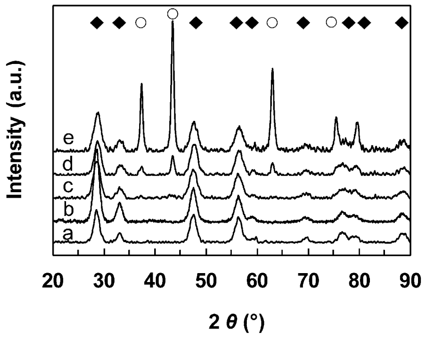

Figure 4. XRD patterns of $CeNi_XO_Y$ nanocompounds: $X=0.02$ (a), 0.3 (b), 0.5 (c), 1 (d), and 5 (e). CeO_2 (◆), NiO (○).

The crystallite sizes of NiO and CeO_2 particles are estimated from the diffraction lines by taking into account the (111), (200), and (220) planes. The average crystallite size of CeO_2 particles is approximately 5 nm (Table 1), which decreases slightly with the Ni content. In the case of NiO particles, the average crystallite size increases slightly from 8 to 11 nm with an increase in the Ni content. It is necessary to recall that the crystallites smaller than 2 nm cannot be examined by using the XRD technique, owing to the detection limit. However, such small-sized NiO nanoparticles have been proved to be present in the $CeNi_XO_Y$ nanocompounds.[43,52]

Analysis by using Raman spectroscopy

The $CeNi_XO_Y$ nanocompounds were also characterized by using Raman spectroscopy. The results show a strong frequency shift and broadening for the first-order (F_{2g}) CeO_2 peak located near 460 cm^{-1} (Figure 5) ascribed to fluorite nanocrystalline CeO_2.[53,54] It shifts to lower frequencies (438 cm^{-1}) compared to those reported previously on Ce–Ni mixed oxides (443 cm^{-1}).[55] This behavior can be ascribed to the solubility of Ni into CeO_2, which is in agreement with the presence of a solid solution.[56] In the present case, the distortion of the lattice and the creation of oxygen vacancies are higher. Secondary peaks at approximately 230 and 330 cm^{-1} ascribed to CeO_2 nanostructures are also observed.[55] The phonon mode at 570 cm^{-1} is characteristic of oxygen vacancies in the CeO_2 lattice.[53,57] The weak shoulders between 500 and 650 cm^{-1} were observed on doped Ce oxides and attributed to oxygen vacancies created due to the incorporation of the dopant.[58] Two modes positioned at 540 and 600 cm^{-1} were ascribed to the local vibrations of different oxygen vacancy (V_O) complexes. The mode at 600 cm^{-1} originates from the existence of Ce^{3+}–V_O complexes in the CeO_2 lattice.[56] Thus, the broad NiO signal at approximately 520 cm^{-1} cannot be well detected, because of a shadowing effect by the long tail of the first-order CeO_2 peak.[59] However, for the low Ni content, two peaks at 540 and 620 cm^{-1} are observed.

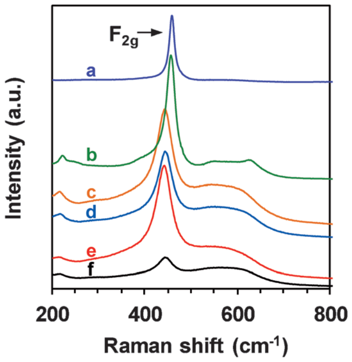

Figure 5. Raman spectra of $CeNi_XO_Y$ nanocompounds: $X=0$ (a, CeO_2), 0.02 (b), 0.3 (c), 0.5 (d), 1 (e), and 5 (f).

Analysis by using H_2 temperature-programmed reduction

The profiles of the temperature-programmed reduction (TPR) in H_2 of $CeNi_XO_Y$ nanocompounds are shown in Figure 6. For a low Ni content ($X=0.3$), one reduction peak ascribed to the Ni species is observed at approximately 270 °C. When the Ni/Ce molar ratio increases from 0.02 to 1, a main reduction peak at approximately 370 °C becomes more intense and shifts slightly toward a higher temperature of 390 °C. The TPR analysis of CeO_2 reveals two peaks at approximately 500 and 820 °C, and thus the reduction peak obtained at approximately 820 °C is assigned to the reduction of bulk Ce^{4+} to Ce^{3+}.

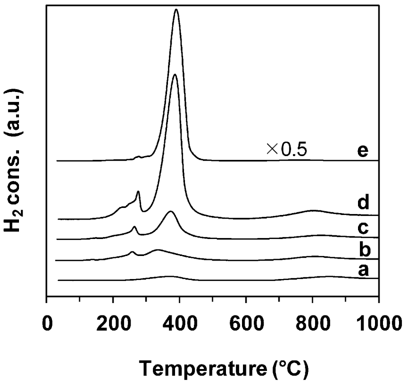

Figure 6. Temperature-programmed reduction profiles of $CeNi_XO_Y$ nanocompounds: $X=0.02$ (a), 0.3 (b), 0.5 (c), 1 (d), and 5 (e).

The in situ treatment of $CeNi_XO_Y$ nanocompounds in H_2 leads to the formation of $CeNi_XH_ZO_Y$ nano-oxyhydride catalysts. The treatment conditions have been optimized in our former papers. To activate the Ni species in the small NiO nanoparticles and/or in the Ce–Ni solid solution, the appropriate treatment temperature in H_2 corresponds to the first TPR peak at approximately 270 °C. Further investigation revealed that a higher reduction temperature of approximately 370 °C cannot improve the catalytic activity; on the contrary, it resulted in a decrease in the ethanol conversion at low temperatures under the SRE reaction conditions.[41,42] In addition to this, chemical titration of the hydrogen species stored in the solids has shown that $CeNi_XO_Y$ nanocompounds can store a large amount of hydrogen and the Ni content affects the hydrogen storage capacity of $CeNi_XO_Y$ compounds.[47,48] The $CeNi_1O_Y$ sample is found to store the largest amount of reactive and extractable hydrogen of all the $CeNi_XO_Y$ series of catalysts. This could well explain the optimum catalytic behavior of the $CeNi_1H_ZO_Y$ catalyst for the product distribution and the highest ΔT_R obtained in the OSRE reaction. To understand the process of hydrogen storage in the catalyst, it has been proposed that H_2 endures the heterolytical dissociation at an anionic vacancy and an O^{2-} species of the mixed oxide [Eq. (8)].

$$\begin{aligned} & O^{2-}M^{n+}\square + H_2 \rightarrow OH^{-}M^{n+}H^{-} \\ & \square \text{ represents an anionic vacancy} \qquad (8) \\ & M^{n+} \text{ represents a cation} \end{aligned}$$

It has already been pointed out that the metallic Ni species can adsorb H_2.[60] Thus, for $CeNi_XO_Y$ nanocompounds, in addition to the heterolytical route described above, the homolytic dissociation of H_2 on Ni^0 species should be considered and different hydrogen species could coexist. However, the in situ

XRD analysis in H_2 does not confirm the presence of Ni^0 species in the $CeNi_1O_Y$ solid at 250 °C after 10 h until the treatment temperature increases to 300 °C.[28]

For the reduction temperatures lower than 600 °C, a linear relationship can be established between the total H_2 consumption during TPR and the Ni content of $CeNi_XO_Y$ nanocompounds (Figure 7), which indicates that H_2 is completely consumed and reduces the Ni species in this range of temperatures. Moreover, the reduction peak at low temperature was attributed to the Ni species present in 1) the solid solution and/or 2) small NiO particles, which are easily reducible; however, with the simultaneous reoxidation of a part of these species through the reduction of the Ce^{4+} cations in the proximity to the Ce^{3+} cations as the existence of a redox system was established [Eqs. (9) and (10)],[46,52] larger NiO crystallites are reduced when the temperature is increased.

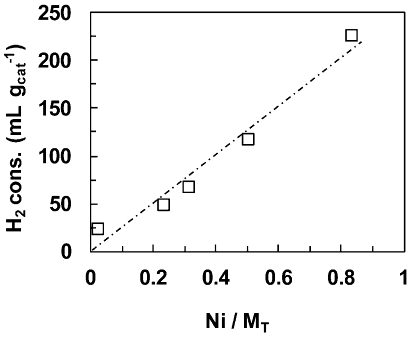

Figure 7. H_2 consumption in temperature-programmed reduction as a function of the Ni content of $CeNi_XO_Y$ nanocompounds.

$$Ni^{2+} + O^{2-} + H_2 \rightarrow Ni^0 + H_2O + \square \qquad (9)$$

$$2\,Ce^{4+} + Ni^0 \leftrightarrow 2\,Ce^{3+} + Ni^{2+} \qquad (10)$$

The reduction peak at approximately 270 °C confirms that this peak ascribes to the Ni species in small NiO nanoparticles and/or in the solid solution. This phenomenon has been verified for different Ni contents. Thus, the $CeNi_XO_Y$ nanocompounds with a large amount of small-sized NiO and CeO_2 nanoparticles can improve the strong interactions between the Ni and Ce species, which enables the mixed oxides to be easily and reversibly reduced and reoxidized.

Characterization of the $CeNi_XH_ZO_Y$ nano-oxyhydride catalysts

Analysis by using inelastic neutron scattering

The introduction of hydride species into the solid is shown here by using inelastic neutron scattering (INS).[61] The H_2 treatment generates an increase in the INS spectrum level as well as the emergence of new peaks associated with hydrogen vibration bands. To observe more precisely the hydrogen species created during the activation treatment in H_2, in Figure 8 the INS spectrum of the corresponding $CeNi_XO_Y$ (calcined) compound has been subtracted from that of the $CeNi_XH_ZO_Y$ compound (treated in H_2 at 250 °C). The hydrogen species with the hydride nature ascribed to the peak at approximately 460 cm^{-1} appear clearly after a treatment in H_2 at 250 °C. The large band at approximately 870 cm^{-1} observed for the $CeNi_1H_ZO_Y$ compound was assigned to the hydrogen species in the interaction with metallic Ni^0 species.[61,62] Even if no Ni^0 species is observed by using XRD, some small particles could still exist, because such small particles are beyond the detection limit of the XRD technique. However, the concentration of this last hydrogen species disappear at Ni/Ce = 0.5 (Figure 8), which is in agreement with the existence of a high proportion of the solid solution of Ce and Ni in this compound.[46]

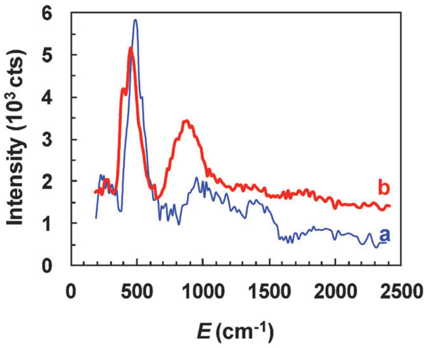

Figure 8. Inelastic neutron scattering spectra of $CeNi_XH_ZO_Y$ catalysts obtained after a treatment in H_2 at 250 °C: a) $X = 0.5$ and b) $X = 1$ (with the subtraction of the background).

Characterization of carbon formed

Analysis by using Raman spectroscopy

In the SRE reaction, the homogeneous filamentous carbon can contribute to the catalytic stability.[43] Because of the small amount of carbon deposited during the reaction, Raman spectroscopy is used, which is the most available and powerful technique to characterize the carbonaceous materials.[63–65] As shown in Figure 9, two main peaks, known as the D band and G band, are visible regardless of the Ni content of the catalyst.

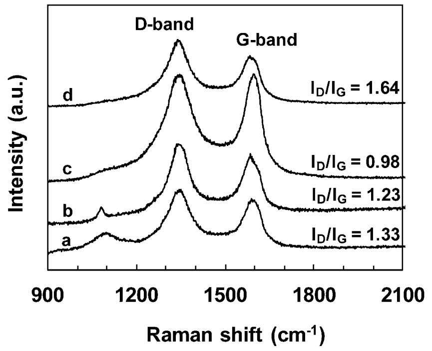

Figure 9. Raman spectra of the carbon species formed on $CeNi_XH_ZO_Y$ nano-oxyhydride catalysts during the oxidative steam reforming of ethanol reaction: $X = 0.3$ (a), 0.5 (b), 1 (c), and 5 (d).

Notably, the carbon deposit without acid treatment in the present result provides information obtained from the spent catalyst. The D band observed between 1343 and 1350 cm^{-1} is ascribed to the vibration of the sp^3 hybridized carbon atom with the dangling bonds in the disordered carbonaceous species, whereas the G band observed between 1586 and 1595 cm^{-1} is ascribed to the stretching mode of the sp^2 hybridized carbon atom in the ordered graphite. Comparisons of the frequency shift between carbon nanotubes (CNTs) and carbon nanofibers (CNFs) were reported, and only small differences could be observed. The D band was obtained at 1350 cm^{-1} for CNFs and 1355 cm^{-1} for CNTs, whereas the G band was observed at 1592 cm^{-1} for CNFs and 1582 cm^{-1} for CNTs.[66] The excellent stability of the $CeNi_XH_ZO_Y$ catalysts is certainly due to the formation of the filamentous carbon species, which probably relate to the CNFs and/or CNTs, although this hypothesis requires more proofs from other characterizations, such as TEM and temperature-programmed oxidation (TPO).

The intensity ratio I_D/I_G can be defined as a measure of the degree of graphitization. Hence, I_D/I_G is characteristic of the degree of order of the carbon materials.[67] The smaller the I_D/I_G ratio, the higher the degree of order of the substances. The I_D/I_G ratios do not depend monotonously on the Ni content, but show the minimum value for the $CeNi_1H_ZO_Y$ catalyst in a decreasing order of 1.64 $(X=5) > 1.33$ $(X=0.3) > 1.23$ $(X=0.5) > 0.98$ $(X=1)$. Thus, the optimal behavior of the $CeNi_1H_ZO_Y$ catalyst ascribed to both the catalytic performance and the physicochemical property could be due to the formation of fibrous carbon (CNTs and/or CNFs) with the highest degree of graphitization.

Analysis by using O_2-TPO

To gain insight into the nature of the carbon species formed on the $CeNi_1H_ZO_Y$ catalyst, TPO is used to evaluate the nature of carbon structure, that is, whether it is amorphous and/or graphitic in nature (Figure 10). It has already been well established in the literature that the types of carbonaceous species can be identified by the TPO peaks related to different reactivities toward oxidation. It is immediately apparent that no relevant peak ascribed to amorphous carbon is observed at temperatures lower than 400 °C; this is highly reactive toward O_2 and easily oxidized from the Ni surface. The carbon species formed on the $CeNi_1H_ZO_Y$ catalyst is graphitic in nature, which clearly indicates an intense oxidation peak at 603 °C. In TPO analysis, temperatures at approximately 510 °C were ascribed to the single-walled carbon nanotubes whereas temperatures at approximately 610 °C were ascribed to the multiwalled carbon nanotubes. CNFs were affirmed to burn off in lower temperature range than did single-walled carbon nanotubes.[64,67,68] Compared to the TPO profile of the carbon species generated on the $CeNi_1O_Y$ catalyst under the SRE reaction conditions,[43] a narrower peak is found that shifts toward a higher oxidation temperature, which suggests that the carbon formed on the $CeNi_1H_ZO_Y$ catalyst under the OSRE reaction conditions is more graphitic in structure. Therefore, the carbon formed during the present process can be observed as an added value, as CNFs and multiwalled carbon nanotubes are strategic materials in various fields and are interesting catalyst support materials for diverse catalyst applications.[68]

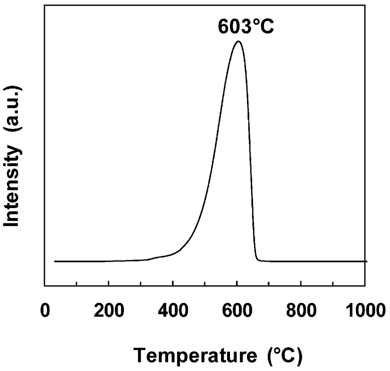

Figure 10. Temperature-programmed oxidation profile of the carbon species formed on the $CeNi_1H_ZO_Y$ nano-oxyhydride catalyst during the oxidative steam reforming of ethanol reaction.

Analysis by using TEM

TEM is used to study the morphology of the carbon species formed (Figure 11). The carbon filaments are clearly observed on the $CeNi_1H_ZO_Y$ catalyst after the OSRE reaction, which is in accordance with the results of TPO analysis. Moreover, Ni particles are observed at the tip of the carbon filaments. Such types of filamentous carbon species have already been reported as the benefit to the catalytic stability for the SRE reaction on the $CeNi_1O_Y$ nanocompound.[43] The carbon filaments are composed of graphitic sheets, and the graphitic structure is shown in Figure 11. This result is in good agreement with the Raman spectrum of the carbon species formed on the $CeNi_1H_ZO_Y$ catalyst, in which the G band observed at 1595 cm^{-1} is ascribed to the stretching mode of the sp^2 hybridized carbon atom in the ordered graphite. Moreover, the $CeNi_1H_ZO_Y$ catalyst has the minimum I_D/I_G ratio, which corresponds to a higher degree of order of substances.

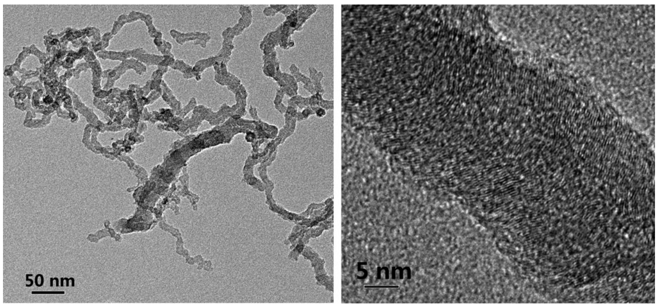

Figure 11. TEM images of the spent $CeNi_1H_ZO_Y$ nano-oxyhydride catalyst after the oxidative steam reforming of ethanol reaction. The 5 nm scale image focuses on carbon species.

Active site modeling

The ethanol dehydrogenation step requires the abstraction of hydrogen species from alcohol. As it has often been remarked that the abstraction of hydrogen from alcohol is the rate-determining step, the ability of the solid to accept hydrogen is an important factor. The variation in the temperature measured is mainly attributed to the reaction between the hydride species of the solid and O_2 (exothermic), and it depends on the concentration of hydrogen stored in the solid in the hydride form.[47] This phenomenon enables the decrease in the oven temperature. A part of hydride species formed from ethanol react with O_2, which provides chemical energy and maintains the catalytic reaction. The reaction is sustainable because hydride species are provided by ethanol. An active site involving an anionic vacancy and an O^{2-} species of the solid can be envisaged for the heterolytic dissociation of ethanol [Eq. (11)], as it has been proposed for the heterolytic dissociation of H_2 [Eq. (8)].

$$O^{2-}M^{n+}\square + C_2H_5OH \rightarrow OH^{-}M^{n+}H^{-} + CH_3CHO \qquad (11)$$

Such a site has already been modeled by an ensemble of two cations in the close interaction.[28] It has been shown in the laboratory that three coordinatively unsaturated sites (^{3}M) are a prerequisite condition for alkadiene hydrogenation activity and different ensembles $^XM{-}^YM'$ (in which X and Y are the number of unsaturations, i.e., anionic vacancies on each cation) have been proposed to be the active sites; each elementary ensemble is associated with a particular reaction. Depending on the unsaturation degree of this active site, ethanol transformation can lead to different products. With a low unsaturation degree (one anionic vacancy), CH_3CHO and H_2 can be obtained through the heterolytic abstraction of hydrogen. On a site with a higher unsaturation degree obtained after a treatment in H_2 at 250 °C, ethanol can be transformed into H_2 and other products.[28] This is in agreement with the observed increase in O vacancies induced by doping CeO_2 with Ni[15,55] even if the existence of a hydride species has not been envisaged.[15]

Conclusions

We have developed a novel catalytic technology to support a sustainable H_2 production from ethanol and water at room temperature. We report highly efficient and stable $CeNi_XH_ZO_Y$ nano-oxyhydride catalysts for the oxidative steam reforming of ethanol. A facile coprecipitation method is used to prepare the $CeNi_XO_Y$ nanocompounds, which possess a high proportion of active Ni species in small-sized NiO nanoparticles and/or in the solid solution and can be reduced and reoxidized easily and reversibly because of the existence of strong interactions between the Ni and Ce cations. The inelastic neutron scattering characterization confirms that the hydride species are introduced into the $CeNi_XO_Y$ nanocompounds to fabricate $CeNi_XH_ZO_Y$ nano-oxyhydride catalysts after an in situ treatment in H_2 at 250 °C. This new technology enables us to save energy by combining the exothermic chemical reaction between the hydride species stored in the $CeNi_XH_ZO_Y$ catalysts and O_2 with the exothermic ethanol partial oxidation. Hence, a huge variation in the temperature between the catalyst bed and the oven can be observed. Such a unique advantage can completely convert ethanol and produce H_2, with the need of only a small amount of extra energy, and it lowers the oven temperature down to 60 °C. $CeNi_XH_ZO_Y$ catalysts show excellent catalytic stability owing to the graphitic filamentous carbon species formed during the reaction. The Ni content has a significant effect on the product distribution, whereas the activity is ascribed to the hydrogen storage capacity of the solid depending on the Ni content. The $CeNi_1H_ZO_Y$ nano-oxyhydride is proved to be the best catalyst in the series analyzed. Complete ethanol conversion and 45 % H_2 molar fraction in all the gas phase products are achieved at 345 °C when the oven temperature is at only 60 °C. In addition, a small amount of carbon is formed (with a formation rate of 28 $mg\,h^{-1}\,g_{cat}{}^{-1}$) after 75 h of the reaction. This is the best result that has ever been reported for a low-cost catalytic system.

Experimental Section

Catalysts preparation

The $CeNi_XO_Y$ nanocompounds were prepared by using the coprecipitation method. The Ni and Ce nitrate solutions (0.5 $mol\,L^{-1}$) were coprecipitated with triethylamine. After filtration, the solids were dried at 100 °C and finally calcined in air at 500 °C for 4 h.

Catalytic reaction

The catalytic reaction was performed under the atmospheric pressure in a fixed-bed quartz reactor (inner diameter 8 mm) fitted in a programmable oven. The catalyst (30 mg) was previously treated in situ in H_2 at 250 °C for 10 h. The water–ethanol mixture with a stoichiometric molar ratio of 3 was pumped and vaporized in the heating chamber. The gas stream of $H_2O/EtOH/O_2/N_2 = 3{:}1{:}1.6{:}1.3$ was then fed to the reactor, with a total flow rate of 60 $mL\,min^{-1}$. The outlet gases were analyzed online with a TRACE GC ULTRA gas chromatograph equipped with a thermal conductivity detector and a flame ionization detector.

The reactants were introduced in a specific order, and O_2 was fed in the last to avoid the immediate reoxidation of the oxyhydride. After all the reactants were fed, the reaction could be activated at a certain temperature, depending on the ability of the oxyhydride catalyst to react with O_2. The heat of the oven was reduced as soon as the measured reaction temperature started to increase drastically, and the variation in the reaction temperature was recorded.

Catalytic performances were measured by calculating ethanol conversion (X_{EtOH}) and product molar composition (C_i) (dry basis) [Eqs. (12) and (13)].

$$X_{EtOH} = \frac{n_{EtOH,in} - n_{EtOH,out}}{n_{EtOH,in}} \times 100\,\% \qquad (12)$$

$$C_i = \frac{n_i}{\sum_{products} n_i} \times 100\,\% \qquad (13)$$

Characterizations

The Ni and Ce contents (in wt%) were analyzed by using inductively coupled plasma-mass spectrometry (CNRS, Service Central d'Analyse, Vernaison, France). For $CeNi_XH_ZO_Y$ catalysts, the Ni/M_T molar ratio is the Ni molar proportion in all the metals ($M_T = X+1$; $Ni/M_T = X/(X+1)$).

The BET surface area was measured by using N_2 physisorption at 77 K with a Micromeritics Tristar II 3020 surface area and porosimetry analyzer. Samples were previously outgassed under vacuum at 150 °C for 3 h.

XRD analysis was performed with a Bruker D8 Advance X-ray diffractometer equipped with a fast detector-type LynxEye with a copper anticathode. The XRD patterns were registered at $2\theta = 20–90^\circ$, with a measured step of 0.02°, and the integration time was set at 0.3 s. The crystallite size was calculated by using the Scherrer equation.

H_2-TPR was performed with a Micromeritics AutoChem II chemisorption analyzer, and the H_2 consumption was measured with a thermal conductivity detector. The sample (50 mg) was treated in a 5 vol% H_2–95 vol% Ar mixture, with a flow rate of 30 $mL\,min^{-1}$. The temperature was increased to 1000 °C, with a heating rate of 10 $^\circ C\,min^{-1}$.

O_2-TPO was performed with a Micromeritics AutoChem 2920 chemisorption analyzer. The sample was treated in a 5 vol% O_2–95 vol% He mixture, with a flow rate of 50 $mL\,min^{-1}$. The temperature was increased to 1000 °C, with a heating rate of 5 $^\circ C\,min^{-1}$. The desorption species from the sample were traced by using an OmniStar GSD 300 O mass spectrometer.

INS experiments were conducted with the IN1 BeF spectrometer at the Institut Laue–Langevin, Grenoble, France. The solid (36 g) was placed in a stainless steel container and treated in high purity H_2 (10 h). INS analysis was performed at 10 K with a Cu monochromator. The scattering cross section is much greater for H_2 [80 barn ($1\ barn = 10^{-28}\ m^2$)] than for other elements (5 barn); therefore, INS emphasizes the motions of hydrogen species.

The Raman spectra were recorded on a LabRam Infinity Raman spectrometer (Horiba Jobin Yvon) using a visible laser with an output laser power of $\lambda = 532$ nm at RT.

TEM images were obtained with a FEI Tecnai G2 20 transmission electron microscope operating at an acceleration voltage of 200 kV. The sample was ultrasonically dispersed in acetone, and then drops of the suspension were placed on a copper grid-supported transparent carbon film.

The amount of carbon formed was determined by measuring mass variation.

Acknowledgements

W.F. gratefully acknowledges a grant from Erasmus Mundus Tandem. C.P. gratefully acknowledges a grant from the French Ministry. A sincere appreciation is dedicated to the Institut Laue–Langevin, Grenoble, France, for the financial support of the INS experiments and to the help of Dr. A. Ivanov (for IN1). The authors thank Ms. L. Burylo (for XRD), Mr. O. Gardoll (for TPR), and Mr. J.C. Morin (for Raman spectroscopy) from the Unité de Catalyse et Chimie du Solide and Mr. A. Addad (for TEM) from the Centre Commun de Microscopie of the University of Lille, "plateau technique de la Fédération Chevreul CNRS FR 2638", for their valuable technical help. The Fonds Européen de Développement Regional, CNRS, Région Nord Pas-de Calais, and Ministére de l'Education Nationale de l'Enseignement Supérieur et de la Recherche are also acknowledged for the funding of XRD analysis.

Keywords: ethanol · hydrogen · nickel · oxyhydride · sustainable reactions

[1] G. A. Deluga, J. R. Salge, L. D. Schmidt, X. E. Verykios, *Science* **2004**, *303*, 993 – 997.
[2] A. Midilli, M. Ay, I. Dincer, M. A. Rosen, *Renewable Sustainable Energy Rev.* **2005**, *9*, 273 – 287.
[3] M. Momirlan, T. N. Veziroglu, *Int. J. Hydrogen Energy* **2005**, *30*, 795 – 802.
[4] V. A. Goltsov, T. N. Veziroglu, L. F. Goltsova, *Int. J. Hydrogen Energy* **2006**, *31*, 153 – 159.
[5] K. Christopher, R. Dimitrios, *Energy Environ. Sci.* **2012**, *5*, 6640 – 6651.
[6] J. A. Turner, *Science* **2004**, *305*, 972 – 974.
[7] M. Ni, D. Y. C. Leung, M. K. H. Leung, *Int. J. Hydrogen Energy* **2007**, *32*, 3238 – 3247.
[8] R. M. Navarro, M. C. Sanchez-Sanchez, M. C. Alvarez-Galvan, F. d. Valle, J. L. G. Fierro, *Energy Environ. Sci.* **2009**, *2*, 35 – 54.
[9] D. Chen, L. He, *ChemCatChem* **2011**, *3*, 490 – 511.
[10] L. He, D. Chen, *ChemSusChem* **2012**, *5*, 587 – 595.
[11] S. Dutta, *RSC Adv.* **2012**, *2*, 12575 – 12593.
[12] N. Bion, D. Duprez, F. Epron, *ChemSusChem* **2012**, *5*, 76 – 84.
[13] L. V. Mattos, G. Jacobs, B. H. Davis, F. B. Noronha, *Chem. Rev.* **2012**, *112*, 4094 – 4123.
[14] E. Y. García, M. A. Laborde, *Int. J. Hydrogen Energy* **1991**, *16*, 307 – 312.
[15] G. Zhou, L. Barrio, S. Agnoli, S. D. Senanayake, J. Evans, A. Kubacka, M. Estrella, J. C. Hanson, A. Martínez-Arias, M. Fernández-García, J. A. Rodriguez, *Angew. Chem.* **2010**, *122*, 9874 – 9878; *Angew. Chem. Int. Ed.* **2010**, *49*, 9680 – 9684.
[16] M. Z. Jacobson, W. G. Colella, D. M. Golden, *Science* **2005**, *308*, 1901 – 1905.
[17] J. C. Ruiz-Morales, D. Marrero-Lopez, J. Canales-Vazquez, J. T. S. Irvine, *RSC Adv.* **2011**, *1*, 1403 – 1414.
[18] M. Contestabile, G. J. Offer, R. Slade, F. Jaeger, M. Thoennes, *Energy Environ. Sci.* **2011**, *4*, 3754 – 3772.
[19] J. R. Salge, G. A. Deluga, L. D. Schmidt, *J. Catal.* **2005**, *235*, 69 – 78.
[20] S. N. Hsu, J. L. Bi, W. F. Wang, C. T. Yeh, C. B. Wang, *Int. J. Hydrogen Energy* **2008**, *33*, 693 – 699.
[21] K. Sato, K. Kawano, A. Ito, Y. Takita, K. Nagaoka, *ChemSusChem* **2010**, *3*, 1364 – 1366.
[22] W. Cai, F. Wang, E. Zhan, A. C. Van Veen, C. Mirodatos, W. Shen, *J. Catal.* **2008**, *257*, 96 – 107.
[23] S. M. de Lima, I. O. da Cruz, G. Jacobs, B. H. Davis, L. V. Mattos, F. B. Noronha, *J. Catal.* **2008**, *257*, 356 – 368.
[24] H. Chen, H. Yu, F. Peng, H. Wang, J. Yang, M. Pan, *J. Catal.* **2010**, *269*, 281 – 290.
[25] F. Frusteri, S. Freni, V. Chiodo, S. Donato, G. Bonura, S. Cavallaro, *Int. J. Hydrogen Energy* **2006**, *31*, 2193 – 2199.
[26] E. B. Pereira, P. Ramírez De La Piscina, S. Martí, N. Homs, *Energy Environ. Sci.* **2010**, *3*, 487 – 493.
[27] S. Andonova, C. N. de Ávila, K. Arishtirova, J. M. C. Bueno, S. Damyanova, *Appl. Catal. B* **2011**, *105*, 346 – 360.
[28] C. Pirez, M. Capron, H. Jobic, F. Dumeignil, L. Jalowiecki-Duhamel, *Angew. Chem.* **2011**, *123*, 10375 – 10379; *Angew. Chem. Int. Ed.* **2011**, *50*, 10193 – 10197.
[29] B. Neltner, B. Peddie, A. Xu, W. Doenlen, K. Durand, D. S. Yun, S. Speakman, A. Peterson, A. Belcher, *ACS Nano* **2010**, *4*, 3227 – 3235.
[30] A. Iulianelli, A. Basile, *Catal. Sci. Technol.* **2011**, *1*, 366 – 379.
[31] N. Zhu, X. Dong, Z. Liu, G. Zhang, W. Jin, N. Xu, *Chem. Commun.* **2012**, *48*, 7137 – 7139.
[32] M. Wang, L. Sun, *ChemSusChem* **2010**, *3*, 551 – 554.
[33] R. M. Navarro Yerga, M. C. Álvarez-Galván, N. Mota, J. A. Villoria de La Mano, S. M. Al-Zahrani, J. L. G. Fierro, *ChemCatChem* **2011**, *3*, 440 – 457.

[34] C. Descorme, P. Gallezot, C. Geantet, C. George, *ChemCatChem* **2012**, *4*, 1897 – 1906.
[35] W. Cai, F. Wang, C. Daniel, A. C. van Veen, Y. Schuurman, C. Descorme, H. Provendier, W. Shen, C. Mirodatos, *J. Catal.* **2012**, *286*, 137 – 152.
[36] S. Velu, N. Satoh, C. S. Gopinath, K. Suzuki, *Catal. Lett.* **2002**, *82*, 145 – 152.
[37] R. Guil-López, R. M. Navarro, M. A. Peña, J. L. G. Fierro, *Int. J. Hydrogen Energy* **2011**, *36*, 1512 – 1523.
[38] C. Bianchini, P. Fornasiero, *ChemCatChem* **2012**, *4*, 45 – 46.
[39] G. Frenette, D. Forthoffer, *Int. J. Hydrogen Energy* **2009**, *34*, 3578 – 3588.
[40] P. Leung, A. Tsolakis, J. Rodriguez-Fernandez, S. Golunski, *Energy Environ. Sci.* **2010**, *3*, 780 – 788.
[41] L. Jalowiecki-Duhamel, C. Pirez, M. Capron, F. Dumeignil, E. Payen, *Int. J. Hydrogen Energy* **2010**, *35*, 12741 – 12750.
[42] L. Jalowiecki-Duhamel, C. Pirez, M. Capron, F. Dumeignil, E. Payen, *Catal. Today* **2010**, *157*, 456 – 461.
[43] W. Fang, C. Pirez, M. Capron, S. Paul, T. Raja, P. L. Dhepe, F. Dumeignil, L. Jalowiecki-Duhamel, *RSC Adv.* **2012**, *2*, 9626 – 9634.
[44] S. Yin, Y. Minamidate, S. Tonouchi, T. Goto, Q. Dong, H. Yamane, T. Sato, *RSC Adv.* **2012**, *2*, 5976 – 5982.
[45] H. Li, G. Wang, F. Zhang, Y. Cai, Y. Wang, I. Djerdj, *RSC Adv.* **2012**, *2*, 12413 – 12423.
[46] C. Lamonier, A. Ponchel, A. D'Huysser, L. Jalowiecki-Duhamel, *Catal. Today* **1999**, *50*, 247 – 259.
[47] L. Jalowiecki-Duhamel, *Int. J. Hydrogen Energy* **2006**, *31*, 191 – 195.
[48] L. Jalowiecki-Duhamel, J. Carpentier, A. Ponchel, *Int. J. Hydrogen Energy* **2007**, *32*, 2439 – 2444.
[49] L. Jalowiecki-Duhamel, H. Zarrou, A. D'Huysser, *Int. J. Hydrogen Energy* **2008**, *33*, 5527 – 5534.
[50] M. A. Ebiad, D. R. Abd El-Hafiz, R. A. Elsalamony, L. S. Mohamed, *RSC Adv.* **2012**, *2*, 8145 – 8156.
[51] J. Rass-Hansen, C. H. Christensen, J. Sehested, S. Helveg, J. R. Rostrup-Nielsen, S. Dahl, *Green Chem.* **2007**, *9*, 1016 – 1021.
[52] A. Ponchel, A. Huysser, C. Lamonier, L. Jalowiecki-Duhamel, *Phys. Chem. Chem. Phys.* **2000**, *2*, 303 – 312.
[53] G. Li, R. L. Smith, Jr., H. Inomata, *J. Am. Chem. Soc.* **2001**, *123*, 11091 – 11092.
[54] S.-L. Zhong, L.-F. Zhang, L. Wang, W.-X. Huang, C.-M. Fan, A.-W. Xu, *J. Phys. Chem. C* **2012**, *116*, 13127 – 13132.
[55] L. Barrio, A. Kubacka, G. Zhou, M. Estrella, A. Martínez-Arias, J. C. Hanson, M. Fernández-García, J. A. Rodriguez, *J. Phys. Chem. C* **2010**, *114*, 12689 – 12697.
[56] N. Paunović, Z. Dohčević-Mitrović, R. Scurtu, S. Aškrabić, M. Prekajski, B. Matović, Z. V. Popović, *Nanoscale* **2012**, *4*, 5469 – 5476.
[57] A. Mineshige, T. Taji, Y. Moroi, M. Kobune, S. Fujii, N. Nishi, M. Inaba, Z. Ogumi, *Solid State Ionics* **2000**, *135*, 481 – 485.
[58] M. Palard, J. Balencie, A. Maguer, J.-F. Hochepied, *Mater. Chem. Phys.* **2010**, *120*, 79 – 88.
[59] N. Dharmaraj, P. Prabu, S. Nagarajan, C. H. Kim, J. H. Park, H. Y. Kim, *Mater. Sci. Eng. B* **2006**, *128*, 111 – 114.
[60] C.-j. Liu, J. Ye, J. Jiang, Y. Pan, *ChemCatChem* **2011**, *3*, 529 – 541.
[61] H. Jobic, *Handbook of Heterogeneous Catalysis, 2nd ed.* (Eds.: G. Ertl, H. Knözinger, F. Schüth, J. Weitkamp), Wiley-VCH, Weinheim, **2008**, pp. 971.
[62] L. Jalowiecki-Duhamel, S. Debeusscher, H. Jobic, E. Payen, *Int. J. Nuclear Hydrogen Prod. Appl.* **2009**, *2*, 148 – 158.
[63] P. Serp, E. Castillejos, *ChemCatChem* **2010**, *2*, 41 – 47.
[64] J.-P. Tessonnier, M. Becker, W. Xia, F. Girgsdies, R. Blume, L. Yao, D. S. Su, M. Muhler, R. Schlögl, *ChemCatChem* **2010**, *2*, 1559 – 1561.
[65] M. Inagaki, H. Orikasa, T. Morishita, *RSC Adv.* **2011**, *1*, 1620 – 1640.
[66] Y. Liu, C. Pan, J. Wang, *J. Mater. Sci.* **2004**, *39*, 1091 – 1094.
[67] Y. Kobayashi, M. Sano, *ChemCatChem* **2010**, *2*, 397 – 401.
[68] E. Sairanen, R. Karinen, M. Borghei, E. I. Kauppinen, J. Lehtonen, *ChemCatChem* **2012**, *4*, 2055 – 2061.

Received: January 31, 2013
Revised: February 28, 2013